This article has been accepted for publication in a future issue of this journal, but has not been fully edited. Content may change prior to final publication. Citation information: DOI 10.1109/JSTARS.2021.3106449, IEEE Journal of Selected Topics in Applied Earth Observations and Remote Sensing

Heuristic Path Planning Method for Multistatic UAV-borne SAR Imaging System

Fanyun Xu, *Student Member, IEEE,* Yongchao Zhang, *Member, IEEE,* Rufei Wang, *Student Member, IEEE,* Chenyang Mi, Yin Zhang, *Member, IEEE,* Yulin Huang, *Senior Member, IEEE,* and Jianyu Yang, *Member, IEEE*

***Abstract*—Multistatic unmanned aerial vehicle-borne synthetic aperture radar (MuUAV-SAR) plays an important role in the applications of environmental monitoring and disaster warning because its distributed platforms can provide high-resolution imagery by fusing the multiple measurements. However, the flight paths of the multiple platforms are limited for such an unmanned system since the flight safety and the path length are basic conditions for guaranteeing the effective observation. This paper first studies the observation signal model of MuUAV-SAR imaging system, and then analyzes the factors that determine the imaging resolution, while these factors are all determined by the flight path of UAVs. Secondly, MuUAV-SAR imaging path planning problem is established as a constrained multi-objective optimization problem (CMOP), which considers the navigation and imaging performance of UAV in the process of completing path planning task in detail. For this CMOP, a heuristic search method is proposed to solve it, which can ensure that each step achieves local optimum, and it can also list all feasible solutions to meet the application requirements for selection. Finally, experimental results verify the effectiveness and practicability of the proposed heuristic path planning method.**

***Index Terms*—Synthetic aperture radar, resolution analysis, UAV path planning, MuUAV-SAR imaging.**

I. Introduction

SYNTHETIC aperture radar (SAR) is widely used in disaster warning, structural mapping and marine applications with advantages of day and night, all-weather, wide swath, long-range imaging features [1-9]. However, because of the limitation of the SAR imaging principle, there will be an imaging blind area in the forward-looking area of radar platforms [10-13]. In order to overcome this problem and obtain more observed information from different views, new radar systems, such as bistatic radar and multi-static radar have emerged and became a research hotspot in recent years [14-18]. Compared with the traditional monostatic SAR, the platforms of multi-static SAR system are completely dispersed in space, which can change the relative spatial configuration of each radar platform more flexibly and adjust the flight path to realize the multi-view observation of the region of interest without blind spots. Moreover, by fusing multi-view information of multi-static radar platforms, higher resolution observation images can be obtained in a shorter time [19-24]. Recently, there have been some research on multi-platform data fusion and resolution enhancement of multi-static SAR [24-26]. In [27, 28], the generalized ambiguity function and resolution expression of BiSAR are analyzed and derived, which provides a basis for further deriving the fusion resolution of multi-static SAR [26]. On the basis of [28, 29], the azimuth resolution of the multi-static SAR imaging system with separated transmitters and receivers is deduced according to the distribution regularities of echo in wave number domain, and the feasibility of echo data fusion of multiple radar platforms to improve imaging resolution are verified [21, 27]. Even when the observation time of a single platform is insufficient, MuUAV-SAR can splice the echo data from multiple transmitters to achieve the same high-resolution observation effect, which is the benefit brought by MuUAV-SAR while it also brings more resource consumption. Therefore, it is necessary to optimize the performance requirements and resource consumption.

Compared with airborne and spaceborne SAR, UAV-borne SAR has a shorter radar range and narrower beam coverage [9, 30], it often works in spotlight SAR mode. Higher imaging resolution can be obtained by the accumulation of echo data through long-time observation of the region of interest [29, 31-33]. For MuUAV-SAR imaging system, high imaging resolution is highly dependent on a good path, and it is also very important to comprehensively consider the path distance of multiple platforms, terrain threats and other factors. As a special SAR imaging system, UAV-borne SAR imaging with receiving and transmitting antennas on the same platform is studied in [1, 32-36]. However, the transmitter and receiver are separated in MuUAV-SAR imaging system, which brings higher flexibility to the system, while some problems need to be solved urgently at the same time. In practical application, the flight paths of UAV usually pass through some hills and canyons [37, 38]. And the flying heights of UAVs are limited to some extent, which will cause the line of sight of UAVs to be blocked by obstacles such as hills and forests, and then lead to the missing of echo data. Aiming at the situation that radar line of sight is blocked or echo signal is interfered, the method of signal processing by data extrapolation under the condition of missing data is put forward [39-41]. These methods are also applicable to MuUAV-SAR imaging system. Besides, UAV is also affected by weather, flight performance and other factors during flight, which causing its nonlinear flight path. Researchers proposed some processing methods of echo signal under the condition of nonlinear flight path [17, 42, 43]. When all of the above problems are solved, multi-UAV cooperative high-resolution imaging is feasible. In order

Manuscript received April 30, 2021; revised June 20 and August 3, 2021; accepted August 14, 2021.

The authors are with the School of Information and Communication Engineering, University of Electronic Science and Technology of China, Chengdu 611731, China, and also with the Yangtze Delta Region Institute of UESTC, Quzhou 324000, China. (e-mail:xufanyun110@163.com; zhang_yongchao1@163.com; mswangrufei@163.com; mdq_uestc@163.com; yinzhang@uestc.edu.cn; yulinhuang@uestc.edu.cn; jyyang@uestc.edu.cn).

This article has been accepted for publication in a future issue of this journal, but has not been fully edited. Content may change prior to final publication. Citation information: DOI 10.1109/JSTARS.2021.3106449, IEEE Journal of Selected Topics in Applied Earth Observations and Remote Sensing

to obtain high-resolution imaging of designated areas using MuUAV-SAR imaging system, it is necessary to plan a path as short as possible to guide UAVs to form as large aperture accumulation as possible while avoiding terrain obstacles.

Path planning for UAV to complete specific optical observation or flight task has been extensively studied [44-47]. However, in the existing studies about multistatic SAR imaging, there are few on path planning. In general, most UAV path planning problems are usually modeled as optimization problems, and different intelligent optimization methods are proposed according to different optimization problem models. Some improved algorithms based on Genetic Algorithm (GA), Particle Swarm Optimization (PSO) algorithm and Ant Colony Optimization (ACO) algorithm are common, they usually need to set process parameters artificially, and different process parameters make the final results vary widely and have no regularity [48-51]. Therefore, it is urgent to propose a stable method that can provide a series of feasible paths for flight task executors to choose. It will also make it possible to choose the most suitable path in any application scenario.

We have discussed the problem of UAV path planning for distributed radar imaging preliminarily in [52]. In order to further verify the effectiveness and feasibility of the proposed method, further research is carried out, including the following three aspects: 1. The azimuth resolution is discussed detail combined with MuUAV-SAR imaging model [53]. 2. The analysis of the influence of the weight hyperparameters of the objective function is added. 3. The imaging effects of 2-D scenario targets corresponding to different planned paths are compared. In this paper, the observation geometry model of MuUAV-SAR imaging is established and the echo signal model is then derived in detail, firstly. Secondly, taking a certain transmitter and a receiver in MuUAV-SAR imaging system as an example, the factors that determine azimuth resolution are analyzed. In the mode of spotlight SAR, the effective azimuth angle variations of receivers are taken as a measure of the imaging resolution. Thirdly, the navigation and imaging performance of MuUAV-SAR platforms are taken into consideration and they are clearly defined as a constrained multi-objective optimization problem (CMOP) with three objective functions and two constraints. Finally, a heuristic search method for UAV path planning is proposed. Task executors can select the optimal path from the feasible solution set based on actual application demand. Finally, some path planning results and corresponding imaging results are given, which proves the effectiveness of this method to improve azimuth resolution.

The organization of the rest of this paper is as follows. Section II established the geometric model and echo signal model of MuUAV-SAR imaging system. Section III analyzed azimuth resolution in detail. Section IV combines the navigation and imaging performance of UAVs to establish a CMOP, and a heuristic search method is proposed to solve the optimization problem. Simulation results are shown in Section V. Section VI covers the conclusions.

II. Echo Signal Modeling for MuUAV-SAR Imaging System

In order to realize the modeling of the echo signal model, the geometric observation model is established according to the MuUAV-SAR imaging detection task. Based on the geometric observation model, the echo signal model can be derived.

A. Geometric observation model

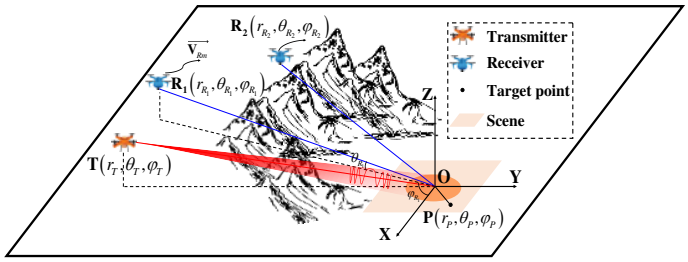

Fig. 1. The geometric observation model of MuUAV-SAR imaging system.

As the geometric observation model shown in Fig.1, a MuUAV-SAR imaging system contains one transmitter and M receivers. The position of transmitter is $\mathbf{T}\left(r_T, \theta_T, \varphi_T\right)$ and the mth receiver is located at $\mathbf{R}_{\mathrm{m}}\left(r_{R_m}, \theta_{R_m}, \varphi_{R_m}\right)$. A reference point in the observation scene is selected as the origin $\mathbf{O}$ and the Cartesian coordinate system is established. The position of target point P can be expressed as $(x_P, y_P, z_P) = (r_P \cos\theta_P \cos\varphi_P, r_P \cos\theta_P \sin\varphi_P, r_P \sin\theta_P)$, where r_P, θ_P, φ_P express radial distance, pitch angle and azimuth angle respectively. The transmitter hovers in the air and ensures that the transmitted beam can always cover the imaging area. Receivers fly along the planned path with the velocity $\overrightarrow{\mathbf{V}}_{R_m}$.

B. Echo signal model

For convenience, assume that UAV radar platforms and imaging scene lie in the same plane as the top view of the geometric observation model shown in Fig. 2. The imaging

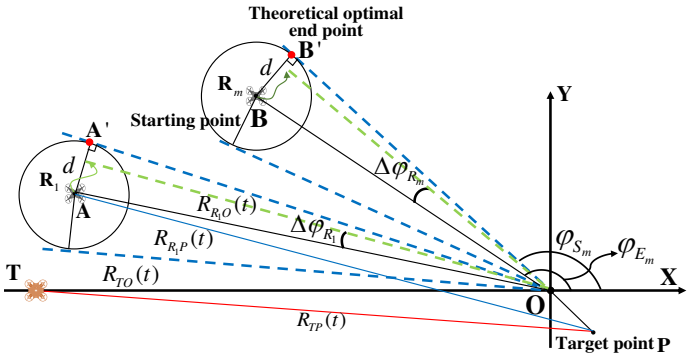

Fig. 2. The top view of the geometric observation model.

system record echo data in spotlight SAR mode. Transmitter radiate linear frequency modulation (LFM) signal is as follow

$$S(\tau) = \mathrm{rect}\left(\frac{\tau}{T_r}\right) \cdot \exp\left(j\pi k\tau^2\right) \cdot \exp\left(j2\pi f_c \tau\right) \quad (1)$$

This article has been accepted for publication in a future issue of this journal, but has not been fully edited. Content may change prior to final publication. Citation information: DOI 10.1109/JSTARS.2021.3106449, IEEE Journal of Selected Topics in Applied Earth Observations and Remote Sensing

where τ is fast time variable, T_r is pulse width, k is chirp rate, and f_c denotes the carrier frequency of the transmitter. After being reflected by the observation scene, the echo signal received by the mth receiver can be expressed as

$$\begin{aligned} S_m(\tau,t) = A\cdot \mathrm{rect}\left(\frac{t}{T_a}\right)\cdot \mathrm{rect}\left[\frac{\tau - R_{mP}(t)/c}{T_r}\right]\cdot \\ \exp\left\{j\pi k[\tau - R_{mP}(t)/c]^2\right\}\cdot \exp\left[-j\frac{2\pi f_c}{c}R_{mP}(t)\right] \end{aligned} \tag{2}$$

where A expresses the amplitude of the echo signal, which is determined by target scattering coefficients and the power attenuation of the transmitted signal in propagation. t, T_a, c represent slow time variable, synthetic aperture time and the velocity of the electromagnetic wave, respectively. $R_{mP}(t) = R_{TP}(t) + R_{R_mP}(t)$ denotes the range history of target point $\mathbf{P}$. Then, through Fourier transform of the above echo signal along the distance direction, the distance frequency domain expression of the echo can be obtained as follows

$$\begin{aligned} S_m(f_\tau,t) = A\cdot \mathrm{rect}\left(\frac{t}{T_a}\right)\cdot \mathrm{rect}\left[\frac{f_\tau}{kT_r}\right]\cdot \exp\left[-j\pi\frac{f_\tau^2}{k}\right]\cdot \\ \exp\left[-j\frac{4\pi}{c}\left(f_{c_m}+f_\tau\right)R_{mP}(t)\right] \end{aligned} \tag{3}$$

where f_τ expresses the frequency variable. Similarly, $R_{mO}(t) = R_{TO}(t) + R_{R_mO}(t)$ expresses the range history of the origin $\mathbf{O}$. Then the echo frequency domain expression of $\mathbf{O}$ can be similarly written as

$$S_{ref}(f_\tau,t) = A\cdot\exp\left(j\pi\frac{f_\tau^2}{k}\right)\cdot\exp\left[j\frac{2\pi}{c}\left(f_c+f_\tau\right)R_{mO}(t)\right] \tag{4}$$

and it is set as a reference function. After completing the pulse compression and range migration correction, the echo frequency domain expression of $\mathbf{P}$ can be expressed as

$$S_m(f_\tau,t) = A\cdot\exp\left\{j\frac{2\pi}{c}\left(f_c+f_\tau\right)\left[R_{mO}(t) - R_{mP}(t)\right]\right\} \tag{5}$$

Further, assuming that the size of the observed scene is much smaller than the distance between the radar platforms and the observed scene center, which can be considered as the far field condition, then we can approximately deduce the range history as

$$\begin{aligned} &R_{mO}(t) - R_{mP}(t) \\ &= |R_{TO}(t) + R_{R_mO}(t)| - |R_{TP}(t) + R_{R_mP}(t)| \\ &\approx x_P\left[\sin\varphi_T(t) + \sin\varphi_{R_m}(t)\right] + y_P\left[\cos\varphi_T(t) + \cos\varphi_{R_m}(t)\right] \end{aligned} \tag{6}$$

Therefore, the frequency domain expression echo of the mth receiver in the beam coverage area Ω can be expressed as

$$S_m(f_\tau,t) = \iint\limits_{(x,y)\in\Omega}\sigma(x,y)\cdot e^{j\cdot[xk_{xm}(f_\tau,t)+yk_{ym}(f_\tau,t)]}dxdy \tag{7}$$

where $\sigma(x,y)$ is the scattering coefficients of target points. $k_{xm}(f_\tau,t), k_{ym}(f_\tau,t)$ are wave number domain variables and they can be denoted concretely as follows

$$\begin{cases} k_{xm}(f_\tau,t) = \dfrac{2\pi}{c}\left(f_c+f_\tau\right)\left[\sin\varphi_T(t) + \sin\varphi_{R_m}(t)\right] \\ k_{ym}(f_\tau,t) = \dfrac{2\pi}{c}\left(f_c+f_\tau\right)\left[\cos\varphi_T(t) + \cos\varphi_{R_m}(t)\right] \end{cases} \tag{8}$$

It can be found in (8) that wavenumber domain variables are related to the frequency variable f_τ and the azimuth angle $\varphi(t)$ of the radar platforms. As sampling time goes on, the azimuth variation and frequency sampling of the radar platforms make the echo data map to spatial spectrum in wavenumber domain. According to the position relationship among the multiple radar platforms, the echo data can be projected into a new coordinate range. The echo data of the MuUAV-SAR can be projected into the wavenumber domain together as

$$s(k_x,k_y) = \sum_{m=1}^{M} A_m^{'} s\left[k_{xm}(f_\tau,t), k_{ym}(f_\tau,t)\right] \tag{9}$$

where $A_m^{'}$ denotes the normalized amplitude of the fused spatial spectrum. Finally, the relationship between the wavenumber domain echo and the PSF can be expressed by matrix Fourier transform (MFT) as

$$\sigma(x,y) = \iint\limits_{(k_x,k_y)\in D_k} s(k_x,k_y)\cdot e^{-j\cdot[xk_x+yk_y]}dk_xdk_y \tag{10}$$

where D_k expresses the boundaries of the fused spatial spectrum area [54].

III. Azimuth resolution analysis for MuUAV-SAR imaging

To analyze the azimuth resolution of MuUAV-SAR imaging system, the relationship between the distribution regularities of spatial spectrum in wavenumber domain and the azimuth resolution is derived. By analyzing the equivalent bandwidth of azimuth direction in wavenumber domain, the factors related to azimuth resolution of MuUAV-SAR imaging system can be indicated.

Based on the analysis in Section II, the range and azimuth resolutions of MuUAV-SAR imaging system are related to the transmitting signal bandwidth and the azimuth angle variations of radar platforms, respectively. The range resolution can be matched with the azimuth resolution by adjusting the bandwidth of the transmitted signal, which will not be further analyzed in this paper. For spotlight SAR, the resolution in azimuth direction can be analyzed in the wavenumber domain [22]. As spatial spectrum in wavenumber domain shown in Fig. 3, assuming that the corresponding sampling points in the wavenumber domain are $K_{start}^{f_{\min}}$ and $K_{end}^{f_{\min}}$ at the beginning and end of echo recording and $f_{\min}$ is the lowest frequency in the frequency band of the transmitted signal. The difference between these two points determines the lowest azimuthal resolution of the system [27]. Therefore, the azimuth

This article has been accepted for publication in a future issue of this journal, but has not been fully edited. Content may change prior to final publication. Citation information: DOI 10.1109/JSTARS.2021.3106449, IEEE Journal of Selected Topics in Applied Earth Observations and Remote Sensing

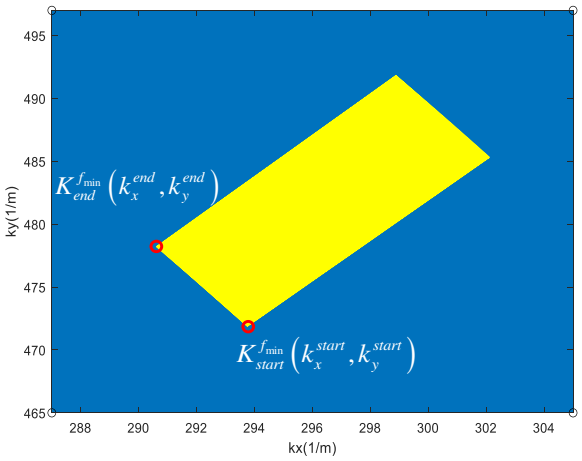

Fig. 3. Spatial spectrum in wavenumber domain.

resolution can be calculated by

$$\begin{aligned}\Delta\rho_{az} &= \frac{2\pi}{\left\|\left\|\overrightarrow{OK_{end}^{f_{\min}}}\right\| - \left\|\overrightarrow{OK_{start}^{f_{\min}}}\right\|\right\|} \\ &= \frac{2\pi}{\sqrt{\left|k_x^{end}-k_x^{start}\right|^2+\left|k_y^{end}-k_y^{start}\right|^2}}\end{aligned} \tag{11}$$

where $\left(k_x^{start},k_y^{start}\right)$ and $\left(k_x^{end},k_y^{end}\right)$ represent the coordinates of the starting point and the ending point. Substitute (8) into (11) and utilize trigonometric function transformation, and then the azimuth resolution expression can be derived as follow

$$\rho_{az}^{m} = \frac{c}{2\left(f_c+f_{\min}\right)}\left[\begin{array}{l}\sin^2\dfrac{\Delta\varphi_T}{2}+\sin^2\dfrac{\Delta\varphi_{R_m}}{2}+ \\ 2\sin\dfrac{\Delta\varphi_T}{2}\sin\dfrac{\Delta\varphi_{R_m}}{2}\cos\dfrac{\beta'}{2}\end{array}\right]^{-\frac{1}{2}} \tag{12}$$

where $\beta' = \beta^{end}+\beta^{start}$, in which $\beta^{end} = \varphi_T^{end}-\varphi_{R_m}^{end}$, $\beta^{start} = \varphi_T^{start}-\varphi_{R_m}^{start}$ represent the bistatic angles corresponding to the starting and ending point of recording echo data, respectively [21]. $\Delta\varphi_T$ and $\Delta\varphi_{R_m}$ are the azimuth change value of the transmitter and receivers relative to the origin **O** in the process of recording echo. Particularly, in the hypothesis of this paper, the transmitter hover in the air, so there is no azimuth variation for the transmitter. The azimuth resolution varies with the movement of the radar receiver platforms, which means $\Delta\varphi_T = 0$. And the movement distance of the radar platform in the synthetic aperture time is much less than the distance between radar platform and the scene center, i.e. $\Delta\varphi_{R_m}$ is close to 0. Therefore, the azimuth resolution can be approximately expressed as

$$\rho_{az}^{m} = \frac{c}{2\left(f_c+f_{\min}\right)\sin\left(\Delta\varphi_{R_m}/2\right)} \approx \frac{\lambda_{\max}}{2\Delta\varphi_{R_m}} \tag{13}$$

where $\lambda_{\max} = c/\left(f_c+f_{\min}\right)$ is maximum wavelength of LFM signal. When the MuUAV-SAR imaging system contains M receivers with small viewing angle differences, the azimuth resolution of the system can be approximately described as

$$\rho_{az} \approx \frac{\lambda_{\max}}{2\sum_{m=1}^{M}\Delta\varphi_{R_m}} \tag{14}$$

The azimuth resolution of the system is jointly influenced by the wavelength of the transmitted signal and the azimuth angle variations of UAV radar platforms in the process of recording echo, and the azimuth angle variations of the radar platforms are the dominant factor for the microwave radar system on UAVs according to (14). In general, larger azimuth variation can help improve azimuth resolution, which will also lead to an increase in path distance. Therefore, the purpose of UAV path planning is to design a path with a large azimuth angle variation and as short as possible through optimization during synthetic aperture time while ensuring the normal flight of UAV.

IV. Optimization Problem Formulation and Path Planning Solving for UAV

Comprehensive analysis the factors such as detection task, navigation constraints and imaging resolution of UAV radar platforms, the UAV path planning problem is established as a CMOP. To solve this CMOP problem, a heuristic optimization algorithm is proposed and the optimal path can be selected from the feasible solution set according to the actual application demand. Finally, the computational complexity of this proposed path planning method is given.

A. Path planning task analysis

The purpose of the path planning for this problem is to develop a method to design a path as short and safe as possible under the condition of meeting the resolution requirement. In the MuUAV-SAR imaging system hypothesized in this paper, the transmitter hovers in the air in the process of recording echoes. Therefore, all the azimuth bandwidth is contributed by the receivers and it is necessary to complete path planning for multiple receiver platforms [55]. A series of feasible solutions can be obtained after optimization, and then screen the most suitable one according to the actual application requirements.

To simulate the specific application requirements, a Digital Elevation Model (DEM) data set of a mountainous area is selected and the interested imaging observation area is identified to complete the path planning of MuUAV-SAR imaging system as Fig. 4 shows. According to the detection requirements, the starting point and the ending point of UAV flight are set, and a reasonable path is planned between the two points. Firstly, in order to reduce resource consumption, it is necessary to limit the distance of UAV flight path. Secondly, in order to ensure UAVs fly safely, the threat of terrain to UAV flight should be considered. Thirdly, combined with the analysis in Section III, to finish azimuth high-resolution imaging, the azimuth angle variations of the receiver platforms relative to the observation scene center will also be considered as one of the objective functions of path planning. Finally, it should be noted that the transmitted signal should be normally received. It requires that the radar line of sight of the receiver is not be obstructed

This article has been accepted for publication in a future issue of this journal, but has not been fully edited. Content may change prior to final publication. Citation information: DOI 10.1109/JSTARS.2021.3106449, IEEE Journal of Selected Topics in Applied Earth Observations and Remote Sensing

by obstacles for a continuous period of time, which will be further explained in Section IV-B.

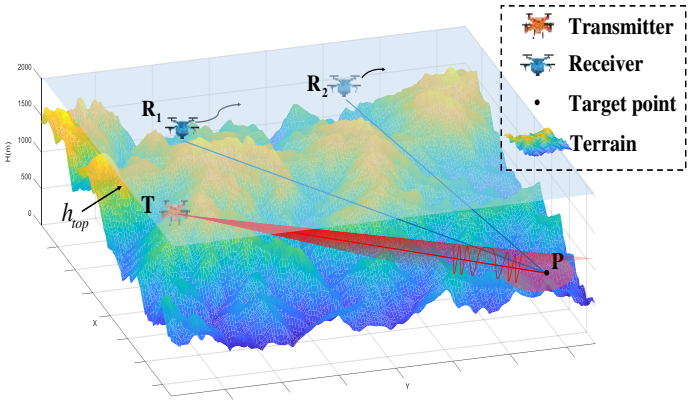

Fig. 4. Path planning model of MuUAV-SAR imaging system.

B. Optimization problem formulation

Fig. 2 shows the top view of the geometric observation model, and suppose that two UAVs act as receivers start flying with the same speed $\overrightarrow{\mathbf{V}}_{R_m}$ from different starting points $\mathbf{A}$ and $\mathbf{B}$ in space. After the same period of time $\tilde{t}$, the two receivers will travel the same distance $d = \left|\overrightarrow{\mathbf{V}}_{R_m}\right| \tilde{t}$, which means the maximum range of motion for UAV receivers during this period $\tilde{t}$ is a circle with the starting point as the center and the length d as the radius. Through simple geometric analysis, if the rays emitted from the center of the scene are tangent to the circle at the red points and set them as the theoretical ending points of the two receivers, the imaging system will be able to obtain the best azimuth resolution in theory according to (14).

Fig. 5 is the 3-D model of UAV path planning and schematic diagram of radar line of sight occlusion analysis. To quantitatively evaluate the navigation and imaging performance in path planning problem, a comprehensive objective function is designed as follow

$$f(\mathbf{x}) = k_1 f_{distance}(\mathbf{x}) + k_2 f_{threat}(\mathbf{x}) + k_3 f_{\Delta\varphi}(\mathbf{x}) \quad (15)$$

where k_1, k_2, k_3 are all constants, which represent the weight of each sub-objective function according to different application requirements. $\mathbf{x}$ represents a specific planning path. The meaning of each sub-objective function is defined in detail as follows.

As shown in Fig. 5 (a), the path between starting point P_{start} and ending point P_{end} is divided into N path points, which are obtained by solving optimization problems and further analysis will introduced in detail in Section IV-C. In practical application, the flight path of UAV cannot be a polyline, so it is necessary to smooth the planned path points by cubic spline interpolation. The detailed steps of cubic spline interpolation can be found in [56]. Then, we can model the path of a UAV receiver as a coordinate sequence

$$L = \left[S_1\left(P_{start}\right), S_2, \ldots, S_N\left(P_{end}\right)\right] \quad (16)$$

where S_i is the ith path point and their 3-D coordinates are $(x_i, y_i, z_i), i = 1, 2, \ldots, N$. Then the whole flight distance can be described as

$$f_{distance}(\mathbf{x}) = \sum_{i=1}^{N-1} \left\|\overrightarrow{S_i S_{i+1}}\right\|, (i = 1, 2, ..., N) \quad (17)$$

where $\|\cdot\|$ is the Euclidean distance between two points. The flight distance $f_{distance}(\mathbf{x})$ should be minimized to avoid excessive energy and mechanical losses.

Considering the physical factors such as the size and inertia of the UAVs, if the distance between UAVs and the terrain is closer, it will be more threatened. Therefore, the terrain threat function in the whole path process can be defined as

$$f_{threat}(\mathbf{x}) = \sum_{i=1}^{N} \frac{1}{h_i(x,y) - z_i(x,y)} \quad (18)$$

where $h_i(x,y), z_i(x,y)$ are the height of the ith path point and the height value of the terrain directly below it. The value of the terrain threat function $f_{threat}(\mathbf{x})$ needs to be as small as possible to ensure that UAVs will not hit the terrain during flight.

In order to ensure that the signal transmitted by the transmitter at a certain path point can be normally received by receivers, it is necessary to judge whether the radar line of sight is blocked by obstacles. As shown in Fig. 5 (b), the spatial triangle formed by two consecutive S_i, S_{i+1} and the target point P is $\triangle\, PS_iS_{i+1}$. The projection of $\triangle\, PS_iS_{i+1}$ in $\mathbf{XOY}$ plane is triangle $\triangle\, P^{'}S_i^{'}S_{i+1}^{'}$, which contains J grid points. For any of the J grid points contained in the region of the triangle $\triangle\, P^{'}S_i^{'}S_{i+1}^{'}$, if all of them satisfy (19), the azimuth angle variation formed by the path points S_i and S_{i+1} can be regarded as effective $\Delta\varphi_{R_m}(\mathbf{x})$

$$z_j(x,y) \geqslant h_{DEM}(x,y), (j = 1, 2, .., J) \quad (19)$$

where $z_j(x,y)$ and $h_{DEM}(x,y)$ are the height of the inner point of the spatial triangle $\triangle\, PS_iS_{i+1}$ and DEM directly above the point (x,y), respectly. Otherwise, if there is a point triangle region $\triangle\, PS_iS_{i+1}$ that does not meet condition (19), this path point will not be included in the point set that contributes to the effective azimuth angle accumulation. The MuUAV-SAR imaging system includes multiple receivers and the azimuth angle variation of each receiver radar platform is beneficial to the improvement of azimuth resolution in the spotlight SAR model. If the effective azimuth angle variation of each receivers is $\Delta\varphi_{R_m}(\mathbf{x})$, then the sub-objective function of azimuth angle can be set as

$$f_{\Delta\varphi}(\mathbf{x}) = \sum_{m=1}^{M} \left\|\Delta\varphi_{R_m}(\mathbf{x}) - \left|\varphi_{E_m} - \varphi_{S_m}\right|\right\| \quad (20)$$

where M denotes the number of receivers in imaging system. $\varphi_{E_m}, \varphi_{S_m}$ represent the azimuth angles corresponding to the starting point and the theoretical ending point of the mth receiver shown in Fig. 2, respectively. On the other hand, h_{top} needs to be set as the upper bound of the path search space to reduce the search range of the solution algorithm as shown in Fig. 4. Finally, the lower resolution cannot obtain effective

This article has been accepted for publication in a future issue of this journal, but has not been fully edited. Content may change prior to final publication. Citation information: DOI 10.1109/JSTARS.2021.3106449, IEEE Journal of Selected Topics in Applied Earth Observations and Remote Sensing

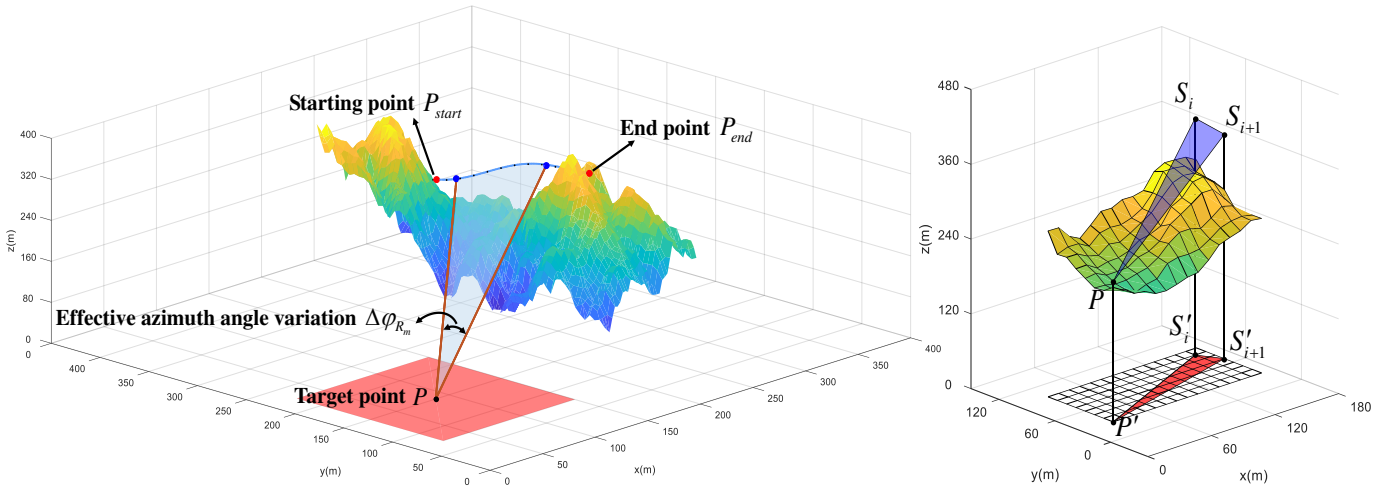

(a) (b)

Fig. 5. 3-D model of UAV path planning and schematic diagram of radar line of sight occlusion analysis.

imaging results, so a resolution threshold $\widehat{\rho}_{az}$ needs to be set as the constraint condition to determine whether there is enough continuous azimuth angle accumulation in the whole path.

Synthesize the above analysis, the path planning optimization problem is modeled as

$$\min f(\mathbf{x}) \quad s.t. \begin{cases} h_i(x,y) \leqslant h_{top} \\ \left\|\overrightarrow{S_k S_{k+n}}\right\| \cdot \cos\theta_{k,k+n} \cdot \dfrac{1}{R_{SP}} \geqslant \dfrac{\lambda}{2\widehat{\rho}_{az}} \end{cases} \tag{21}$$

From S_k to S_{k+n}, there are n continuous path points that can provide effective azimuth variation. And in (21), $\left\|\overrightarrow{S_k S_{k+n}}\right\|$ represents the Euclidean distance of the space vector from S_k to S_{k+n}. $\cos\theta_{k,k+n}$ is the angle between the space vector $\overrightarrow{S_k S_{k+n}}$ and the ground-piston. R_{SP} indicates the distance between the receiver radar platform and the target point. λ is the wavelength of the transmitted signal.

In (15), $f_{distance}(\mathbf{x})$ and $f_{threat}(\mathbf{x})$ comprehensively describe the navigation performance of UAV flight, and $f_{\Delta\varphi}(\mathbf{x})$ represents the resolution performance in azimuth for MuUAV-SAR imaging system. The two constraints jointly ensure the feasibility and effectiveness of the actual flight and imaging detection tasks of UAVs. However, the minimization of navigation performance and imaging performance sub-objective functions are usually contrary to each other. Paths corresponding to longer path distance and higher terrain threat can bring better azimuth resolution, while a better imaging resolution inevitably requires larger azimuth angle variation, which leads to a longer planning path. Therefore, an optimized planning path should achieve a compromise among these sub-objective functions on the premise of satisfying constraints. An path planning solution method needs to be designed to obtain a feasible solution to this problem, so that executors can choose the corresponding weights according to the needs of actual tasks.

C. Path planning for MuUAV-SAR imaging

As analyzed in Section IV-B, it is impossible to achieve optimal navigation performance and imaging performance synchronously, because these two performances are contradictory. Therefore, the proposed method need to automatically indicate the feasible planning paths that meet certain conditions in the feasible solution set, and they represent the tradeoff of each performance in different tasks. Task executors can select the most appropriate path from the solution set to complete the imaging detection task. A greedy search algorithm is proposed to solve this CMOP and the specific algorithm process is listed in TABLE I. The two receivers are independent of each other and path planning can be carried out simultaneously.

Taking a receiver as an example, the main procedure of path planning method is given as follows.

Step 1) Initialization and input of searching algorithm:

Initialization and input are divided into three steps. At first, read DEM data and set the upper bound h_{top} of search space, and put physically unreachable points into closed set $\mathbf{C}$. Path points in the closed set $\mathbf{C}$ cannot be reached and will not be involved in the search process of UAV path planning. Secondly, input the starting point P_{start} and ending point P_{end} of the path planning. Thirdly, set the current point $P_{current}$ as the starting point P_{start}.

Step 2) Setting hyperparameter space $\mathbf{K}$*:*

Based on the actual scene and resolution requirements, the appropriate value range of the hyperparameter $\mathbf{k}$ is set to ensure that the contributions of the three sub-objective functions are similar. Then, according to the requirements of the planning speed, the appropriate value step is set to divide the value space of the hyperparameters, and the value space $\mathbf{K}$ is obtained. Finally, a set of hyperparameters $\mathbf{k} = [k_1, k_2, k_3]^T$ from the value space $\mathbf{K}$ is selected as the weight of each objective function.

Step 3) Searching the extended points:

Take the current point $P_{current}$ as the center and search in all directions. And then find out the points that may

This article has been accepted for publication in a future issue of this journal, but has not been fully edited. Content may change prior to final publication. Citation information: DOI 10.1109/JSTARS.2021.3106449, IEEE Journal of Selected Topics in Applied Earth Observations and Remote Sensing

TABLE I
PATH PLANNING ALGORITHM PROCESS

Algorithm 1: Path planning for MuUAV-SAR imaging system.

Initialization: Add points can not reach to closed set $\mathbf{C}$.
Input: Start point P_{start} and ending point P_{end}.
Set hyperparameter space $\mathbf{K} = \{\mathbf{k}_1, \ldots, \mathbf{k}_\mathrm{I}\}$ where $\mathbf{k}_i = [k_{i1}, k_{i2}, k_{i3}]^T$
for $\mathbf{k}_i$ in $\mathbf{K}$ **do**
  Let $P_{current} = P_{start}$.
  while $P_{current} \neq P_{end}$ **do**
    Add points near current point $P_{current}$ to open set $\mathbf{O}$ (not include points in $\mathbf{C}$).
    Calculate evaluation function $v(\mathbf{x})$ for every point new added in $\mathbf{O}$:

$$f(\mathbf{x}) = k_{i1} f_{distance}(\mathbf{x}) + k_{i2} f_{threat}(\mathbf{x}) + k_{i3} f_{\Delta\varphi}(\mathbf{x})$$
$$h(\mathbf{x}) = discance(P_{current}, P_{end})$$
$$v(\mathbf{x}) = f(\mathbf{x}) + h(\mathbf{x})$$

    Choose point with minimum $v(\mathbf{x})$ value as the next point $P_{current}$.
    Add $P_{current}$ to $\mathbf{C}$.
  end while
  Backtrack $\mathbf{O}$ to get the planned path l_i.
end for
for path l_i **do**
  if $\rho_{li} \leqslant \rho_{\max}$ **do**
    Add path l_i to solution set $\mathbf{L}$.
  end if
end for
Output the planning path set L

arrive at the next moment according to the distribution of the surrounding environment and the velocity vector $\overrightarrow{\mathbf{V}}_{R_m}$ of the UAV receivers which are called extended points P_{extend}. All extended points will be added to the open set $\mathbf{O}$, and they will be used as candidate points for the next planning.

Step 4) Evaluating the extended points:

First, calculate the evaluation function $v(\mathbf{x})$ one by one for the extended points P_{extend} in the open set $\mathbf{O}$. $v(\mathbf{x})$ can be calculated by

$$v(\mathbf{x}) = f(\mathbf{x}) + h(\mathbf{x}) \tag{22}$$

where $f(\mathbf{x})$ is the objective function in (21) and $h(\mathbf{x}) = \left\|\overrightarrow{P_{current}P_{end}}\right\|$ is the Euclidean distance from the current path point $P_{current}$ to the ending point P_{end}. Then, sorting the evaluation functions $v(\mathbf{x})$ of all extended points, and finding out the extended point corresponding to the minimum evaluation function $P_{v(\mathbf{x})_{\min}}$. Finally, take the extended point as the next path point, that is, let $P_{current} = P_{v(\mathbf{x})_{\min}}$ and put $P_{v(\mathbf{x})_{\min}}$ into the close set $\mathbf{C}$ simultaneously. Repeat this step until the planning path reaches the ending point, i.e. $P_{current} = P_{end}$.

Step 5) Backtracking path points:

On the basis of *Step 4)*, trace back the adjacent points in open set $\mathbf{O}$ from the ending point P_{end} to P_{start} and obtain a trace l_i. Perform cubic spline interpolation on trace l_i to obtain the final smooth planned path $\widetilde{l}_i$ and add it to path solution set $\mathbf{L}$ for subsequent screening.

Step 6) Update of weight hyperparameters:

Selecting different weight hyperparameters $\mathbf{k} = [k_1, k_2, k_3]^T$ will obtain different planned paths and correspond to different navigation and imaging performance. First, update a new set of hyperparameters $\mathbf{k}_i = [k_{i1}, k_{i2}, k_{i3}]^T$ from the set $\mathbf{K} = \{\mathbf{k}_1, \ldots, \mathbf{k}_\mathrm{I}\}$, and reset $P_{start} = P_{current}$ to complete initialization. Then, return to *Step 3)* for new path planning.

Step 7) Planning path screening:

Calculate the azimuth resolution of all paths in the planning path set $\mathbf{L}$ and remove paths that do not meet the navigation and imaging resolution from $\mathbf{L}$ according to constraints in (21). And then output the remaining paths in $\mathbf{L}$.

After the above solving steps, a solution set L of the planned path can be obtained. Flight task executors can choose the appropriate path according to the actual demand for the imaging resolution and the path distance.

D. Time Complexity

The time consumption of the proposed method is mainly caused by the following three parts.

This article has been accepted for publication in a future issue of this journal, but has not been fully edited. Content may change prior to final publication. Citation information: DOI 10.1109/JSTARS.2021.3106449, IEEE Journal of Selected Topics in Applied Earth Observations and Remote Sensing

Part 1) Objective function calculation:

Assuming that L search times are required at most in the path planning process, that is, the search length is L. And in each search process, it is necessary to calculate the objective functions of D feasible directions, so the time complexity in the whole path planning process is $D \times L$, where $D < 27$, so the time complexity of one path is $O(L)$. Furthermore, the times of vector $\mathbf{k}_i$ needs to traverse is K, so we need to plan K paths, the actual time complexity of objective function calculation is $O(KL)$.

Part 2) Path points backtracking:

After the path planning is completed, K paths are obtained. Each path retains no more than N path points, we need to backtrack from the ending point to find the path points. Therefore, in the process of backtracking, it is necessary to search the path points for N times for each path, and the time complexity is $O(K)$.

Part 3) Planning path screening

After traversing, we need to calculate the azimuth resolution for all paths, and discard paths do not satisfy constraints (21). The time complexity is $O(K)$.

Through analyzing, it is found that the calculation time length of the *Part 1)* will change with the search times L, and the value of KL is much larger than the value of K. So it can be concluded that the calculation of objective function contribute the main calculation load.

V. Simulation Results

In this section, the performance of the proposed path planning method for MuUAV-SAR is thoroughly verified under different navigation and imaging conditions. First, the joint influence regularities of different weight hyperparameters on imaging performance is analyzed. Then, based on the results of path planning, the imaging resolution performance of point targets are analyzed and the 2-D scenario targets imaging results are compared.

Fig. 6 is the flowchart of path planning and MuUAV-SAR imaging. In the simulation process, set a task requirement and determine the starting point and ending point of the two receivers firstly. Secondly, by using the path planning method proposed in this paper, the feasible path solution set is obtained. Thirdly, select a path to complete the echo generation according to the geometric relationship between the UAV planned path and the imaging scene. Then the echo is projected to the wavenumber domain to complete the fusion of the echoes of two receivers. Finally, the imaging results are completed by using the MFT.

A. Path planning performance analysis

Firstly, a typical mountainous area is selected on the map and the DEM of this area is read as shown in Fig. 10 (a), (c), (e). This DEM actually corresponds to an $1689.69\ m \times 1126.46\ m$ area, where the side length of each grid is $11.26\ m$. Set $h_{top} = 300\ m$ as the upper bound

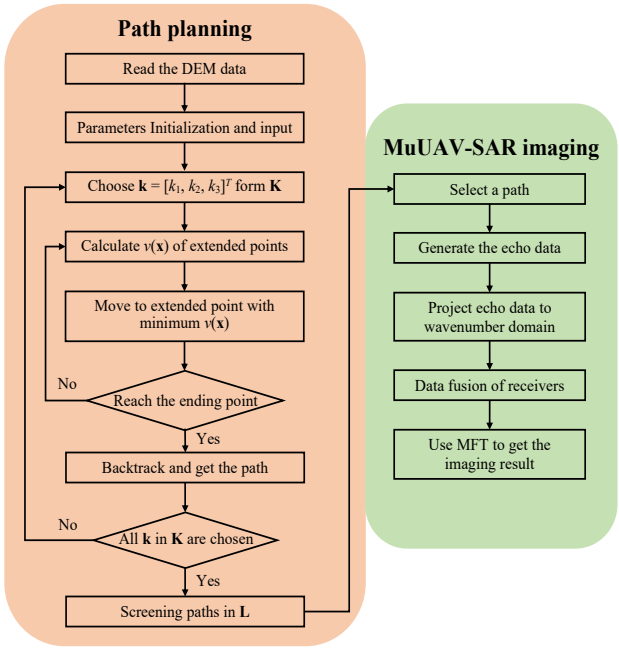

Fig. 6. The flowchart of path planning and MuUAV-SAR imaging.

of spatial path search. Then, a MuUAV-SAR imaging system consisting of one UAV as transmitter and two UAVs as receivers is used to realize cooperatively imaging of a designated area. The imaging scene center is $\mathbf{O}(0,0,0)$. The starting point and ending point of two receivers are located at $P^1_{start}(-980, 237, 85)\ m$, $P^2_{start}(-935, 304, 113)\ m$ and $P^1_{end}(-935, 304, 113)\ m$, $P^2_{end}(-958, 248, 113)\ m$. The hovering position of the transmitter is $\mathbf{T}(-529.2, 0, 33.8)\ m$. To recognize the ground target effectively, the azimuth resolution requirement $\widehat{\rho}_{az}$ in (21) in this experiment is set to $0.5\ m$. Other simulation parameters are listed in the TABLE II. Finally, start path planning using the method proposed.

TABLE II
Parameters of MuUAV-SAR Imaging System

Parameter	Value
UAV transmitter velocity	0 m/s
UAV receiver velocity	5 m/s
Carrier frequency	8 GHz
Bandwidth	800 MHz
Sampling rate	1.2 GHz
Pulse repetition interval (PRI)	500 μs
Pulse width	2 μs

We analyze the influence and regularity of three weight hyperparameters $k_{dis}\,(k_1)$, $k_{thr}\,(k_2)$, $k_{phi}\,(k_3)$ for UAV navigation and imaging performance in optimization model (21). The two weight k_{dis}, k_{phi} take values at intervals of 0.3 between 0 and 4.5 and k_{thr} take values at intervals of 1 between 1 and 5. For the imaging performance here, we only consider the azimuth resolution, which is quantified by the sum of effective azimuth angle variations of all receivers in

This article has been accepted for publication in a future issue of this journal, but has not been fully edited. Content may change prior to final publication. Citation information: DOI 10.1109/JSTARS.2021.3106449, IEEE Journal of Selected Topics in Applied Earth Observations and Remote Sensing

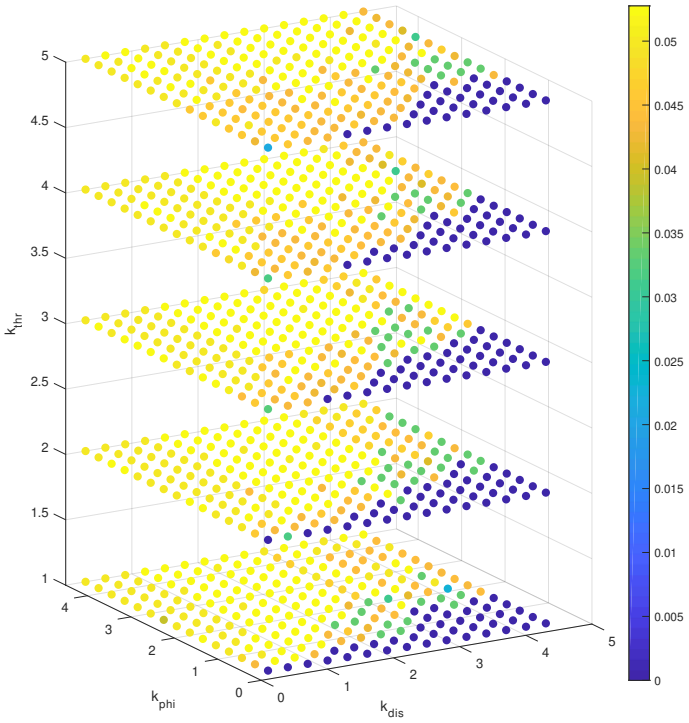

Fig. 7. Influence of weight hyperparameters on imaging performance.

this imaging system according to (14).

Fig. 7 illustrates the influence of different weight hyperparameters on imaging performance. Three-dimensional coordinates respectively represent the values of three weight parameters k_{dis}, k_{thr}, k_{phi}, and the color of each point expresses the quantization of the value of azimuth angle variation according to the colorbar. It is easy to find that the influence of weights k_{dis} and k_{phi} on imaging performance is consistent for different values of k_{thr}. Therefore, it can be concluded that k_{thr} is not the dominant factor for imaging resolution. In order to obtain a path with shorter path distance and better imaging performance, it is necessary to further study the influence regularity of angle weight k_{phi} and distance weight k_{dis}.

Fig. 8 illustrates the distribution regularity of effective azimuth angle variations and path distance when $k_{thr} = 1, 3, 5$. It should be noted that the imaging resolution are limited to some extent in practical application. Based on the constraints in (21), not all the planned path results corresponding to the hyperparameters are effective, so the threshold value is set for screening feasible path. In Fig. 8(a)-(c), the blue transparent plane is the threshold plane drawn by the second constraint in (21), which means that no path meeting the required imaging resolution can be found using the weights corresponding to points below the plane. Therefore, these weight hyperparameters should be discarded. When k_{dis} is small and k_{phi} is large, there is a large stable region, which can easily select more hyperparameters combinations to realize the high-resolution imaging. In Fig. 8(d)-(f), with the increase of weight k_{phi}, the path distance will increase, while the weight k_{dis} increases, the path distance will decrease. Matching and sorting the sub figure in Fig. 8 vertically according to (a) and (d), (b) and (e), (c) and (f), the final feasible solution set can be obtained as shown by the blue circle in Fig. 9 when the requirements of all objective functions are within the expected range.

In Fig. 9, the horizontal axis "Distance" represents the sum of the path distance of the two receivers, while the vertical axis "Angle" represents the sum of the effective azimuth angle variation obtained during the flight of the two receivers. The red and blue points in Fig. 9 are all the remaining feasible paths after screening. The points below the red line can not reach the resolution requirements which need to be discarded. The hyperparameters corresponding to three points A, B and C are selected from these points to complete the path planning, and the results are correspond to path A, B and C in Fig. 10 (a),(c),(e), respectively.

In Fig. 10 (a),(c),(e), black and green solid dots represent the starting point and ending point of path planning respectively. Hovering transmitter and imaging scene center are separately represented by he black diamond and the red square. The red curves represent the part of radar line of sight is blocked by terrain and the blue curves are the part that can form effective azimuth angle variations in flight path. In combination with Fig. 9, it can be concluded that path A has the largest effective azimuth angle variations, but it also brings an increase in path distance. Path B has the shortest path distance but the effective azimuth angle variations are reduced. The navigation and imaging performance of path C is between path A and B, which provides a compromise proposal.

The simulation device is a PC with an i7-10600k 4.1 GHz CPU and 16 GB RAM and the simulation software is a 64-bit MATLAB. Under the above simulation conditions, the total time for all planned path is $836\ s$ and objective function evaluation time for one planned path is $4.56\ s$. It should be noted that the objective function calculation for each planned path provides the major computational load.

B. Imaging resolution performance analysis

Combined with the above solution and analysis of the path planning problem, the path planning method based on greedy thought proposed in this paper list feasible solution sets through weight screening to meet different application requirements. The imaging results of point target simulation and 2-D scenario target simulation are illustrated to verify the imaging performance corresponding to different planned paths. In addition to the simulation parameters listed in TABLE II, signal-to-noise ratio (SNR) is a parameter needs special explanation that the echo signal is corrupted by the additive white gaussian noise (AWGN), and SNR is defined as

$$\text{SNR} = 10\log_{10}\frac{P_s}{\sigma^2} \tag{23}$$

where P_s represents the peak power of the echo signal and σ^2 is the variance of the noise.

1) Point target simulation: The problem is that the MuUAV-SAR imaging system consisting of one transmitter and two receivers needs to fly through the canyon area and finish the imaging task in a designated scene. Then start the

This article has been accepted for publication in a future issue of this journal, but has not been fully edited. Content may change prior to final publication. Citation information: DOI 10.1109/JSTARS.2021.3106449, IEEE Journal of Selected Topics in Applied Earth Observations and Remote Sensing

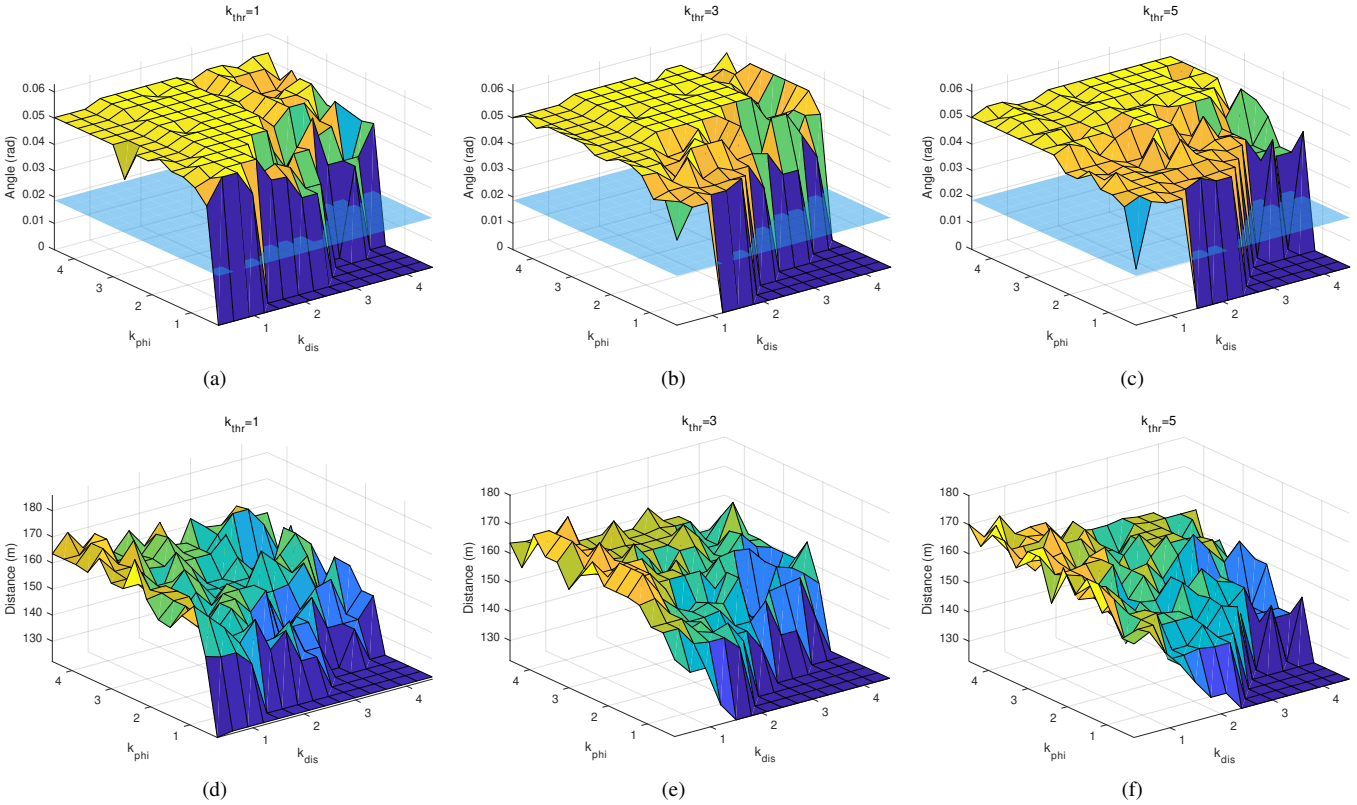

Fig. 8. Distribution regularity of effective azimuth angle variations and path distance when k_{thr} is constant. (a) Angle-k_{dis},k_{phi} ($k_{thr}=1$). (b) Angle-k_{dis},k_{phi} ($k_{thr}=3$). (c) Angle-k_{dis},k_{phi} ($k_{thr}=5$). (d) Distance-k_{dis},k_{phi} ($k_{thr}=1$). (e) Distance-k_{dis},k_{phi} ($k_{thr}=3$). (f) Distance-k_{dis},k_{phi} ($k_{thr}=5$).

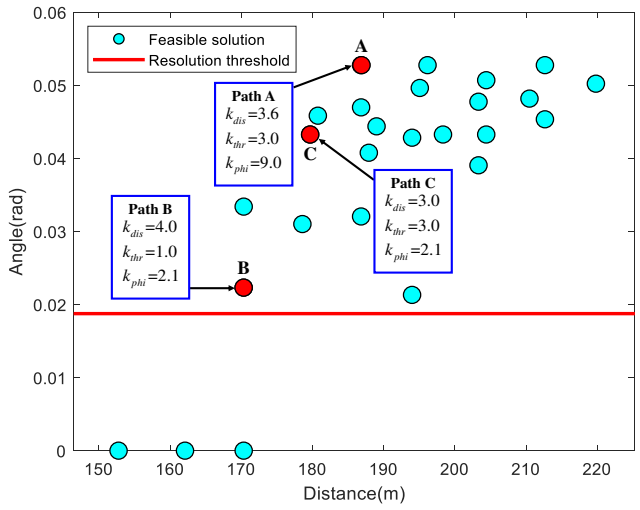

Fig. 9. Distribution of feasible solutions with respect to path distance and azimuth angle variations.

path planning by utilizing the proposed method and the point target imaging simulation is carried out with the planned path.

It is easy to find that a longer distance is necessary to improve the imaging resolution by increasing the azimuth angle variations. And the point with the best imaging performance is point A in Fig. 9 corresponding to path A in Fig. 10. If energy and mechanical losses are considered to shorten the flight path distance, the imaging quality will be sacrificed and the shortest path is the point B in Fig. 9 corresponding to path B in Fig. 10. The path C in Fig. 10 corresponding to point C in Fig. 9 satisfies the compromise between path distance and imaging performance. These three paths are used to complete the point target simulation verification. In the original scene, nine point targets are arranged in three rows and three columns and imaging processing carried out based on (10) [57, 58].

Fig. 10 illustrates the path planning and point target imaging results corresponding to different weight parameters. The navigation and imaging performance quantitative results of specific paths are shown in TABLE III. What needs special explanation is the calculation method of resolution unit area S_{cell} and it represents -3 dB main lobe area. Because of the data fusion of multiple echo signals, the resolution unit is no longer an ellipse but a polygon. The area of the resolution unit can be approximately expressed as

$$S_{cell} = \frac{\pi}{4} \cdot \rho_{\max} \cdot \rho_{\min} \tag{24}$$

where $\rho_{\max}$ and $\rho_{\min}$ represent the longest and the shortest diameter in the resolution unit, respectively [19, 59]. Comprehensive analysis the information shown in Fig. 10 and TABLE III, the path A has a longer distance corresponding to the best imaging performance, while the path B is shortened but the imaging performance is lost. Path C is a compromise between the above two performances.

This article has been accepted for publication in a future issue of this journal, but has not been fully edited. Content may change prior to final publication. Citation information: DOI 10.1109/JSTARS.2021.3106449, IEEE Journal of Selected Topics in Applied Earth Observations and Remote Sensing

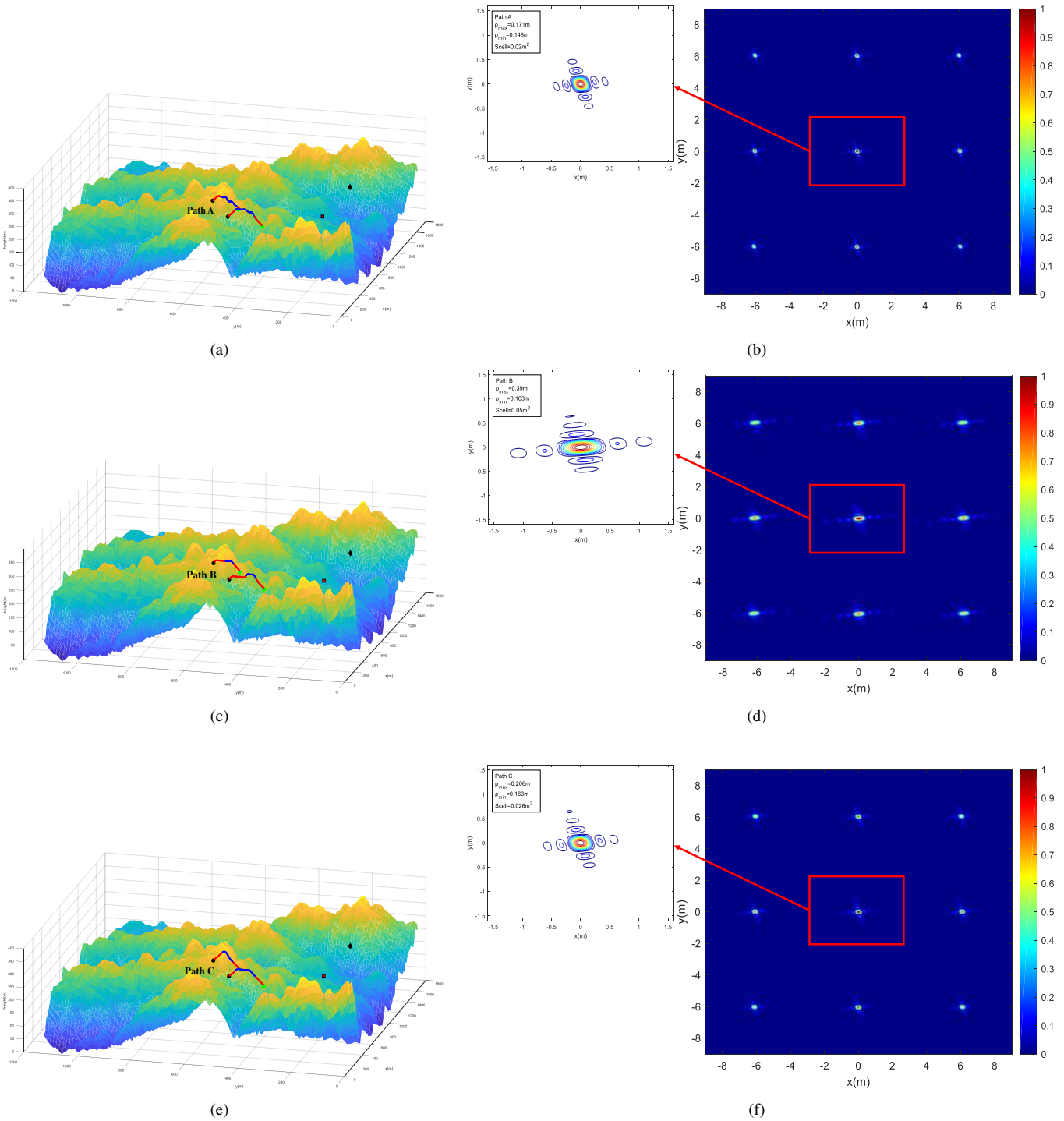

Fig. 10. Path planning and point target simulation results. (a) Path A. (b) Point target imaging result of Path A. (c) Path B. (d) Point target imaging result of Path B. (e) Path C. (f) Point target imaging result of Path C.

This article has been accepted for publication in a future issue of this journal, but has not been fully edited. Content may change prior to final publication. Citation information: DOI 10.1109/JSTARS.2021.3106449, IEEE Journal of Selected Topics in Applied Earth Observations and Remote Sensing

TABLE III
PERFORMANCE COMPARISON OF DIFFERENT PATHS

Indexes \ Path No.		Path A	Path B	Path C
$(k_{dis}, k_{thr}, k_{phi})$		(3.6,3.0,3.9)	(4.2,1.0,2.1)	(3.0, 3.0, 2.1)
Total path distance of T_1 and T_2 (m)		186.8	170.3	179.7
Total terrain threat of T_1 and T_2 (1/m)		0.45	0.51	0.42
Total azimuth angle variation(rad)		0.053	0.022	0.043
PSLR (dB)	ρ_{max}	-13.38	-12.05	-12.87
	ρ_{min}	-13.51	-13.13	-13.35
ISLR (dB)	ρ_{max}	-11.56	-10.01	-11.23
	ρ_{min}	-11.43	-11.08	-11.26

2) 2-D scenario target simulation: To further validate the practicability of the path planning method proposed in this paper, the simulation experiments of the 2-D scenario target are carried out.

Fig. 11 (a)-(c) are the imaging results corresponding to path A, B and C shown in the last sub-section, respectively. Comparing Fig. 11 (a) and (b), Fig. 11 (a) retains more edge information, such as the edge of river bank and fence in area I is clearer. Further, calculate the values of image entropy (IE) of the area I and area II and the result is illustrated beside the imaging results. The IE of these two areas in Fig. 11 (a) are much smaller than that in Fig. 11 (b), and the IE of the selected area in Fig. 11 (c) lies between (a) and (b).

It can be concluded that the clear observation of ground objects can be realized by choosing path A, with a resolution of 0.2m, but it requires two receivers to fly a longer distance. If path B is chosen, the flight distance of UAV can be reduced, but some edge information of ground objects may be lost. Path C can obtain better resolution when the path length is relatively short.

VI. CONCLUSION

In this paper, a MuUAV-SAR imaging system with multiple receivers is proposed and the echo signal model and azimuth resolution are studied firstly. The application of multiple receivers improves imaging resolution, however it will come at the expense of increasing the total flight distance and flight threat. Then, the navigation and resolution performance of UAVs are considered to establish a CMOP. A heuristic search solution method based on greedy thought is proposed to solve this CMOP, which can not only ensure that every step of the search is optimal under certain conditions, but also provide a series of feasible path solution set that meet the requirements for flight task executors to choose. Finally, the imaging simulation results and resolution performance analysis verified the feasibility and practicability of the path planning method.

ACKNOWLEDGMENT

This work was supported in part by the National Natural Science Foundation of China under Grant 61901090, Grant 61901092, and Grant 61671117, in part by the Special Science Foundation of Quzhou. Thanks for providing the help and support and the reviewers for their helpful comments that significantly improved the quality of this paper.

REFERENCES

[1] Mengdao Xing, Xiuwei Jiang, Renbiao Wu, Feng Zhou, and Zheng Bao, "Motion compensation for UAV SAR based on raw radar data," *IEEE Transactions on Geoscience and Remote Sensing*, vol. 47, no. 8, pp. 2870–2883, 2009.

[2] Yongchao Zhang, Yin Zhang, Wenchao Li, Yulin Huang, and Jianyu Yang, "Super-resolution surface mapping for scanning radar: Inverse filtering based on the fast iterative adaptive approach," *IEEE Transactions on Geoscience and Remote Sensing*, vol. 56, no. 1, pp. 127–144, 2018.

[3] Xiaolong Li, Zhi Sun, and Tat Soon Yeo, "Computational efficient refocusing and estimation method for radar moving target with unknown time information," *IEEE Transactions on Computational Imaging*, vol. 6, pp. 544–557, 2020.

[4] Philipp Bernhard, Simon Zwieback, Silvan Leinss, and Irena Hajnsek, "Mapping retrogressive thaw slumps using single-pass TanDEM-X observations," *IEEE Journal of Selected Topics in Applied Earth Observations and Remote Sensing*, vol. 13, pp. 3263–3280, 2020.

[5] Weibo Huo, Yuhsuan Huang, Jifang Pei, Qian Zhang, Qin Gu, and J.M. Yang, "Ship detection from ocean SAR image based on local contrast variance weighted information entropy," *Sensors*, vol. 18, pp. 1196, 04 2018.

[6] Zhi Sun, Xiaolong Li, Guolong Cui, Wei Yi, and Lingjiang Kong, "Hypersonic target detection and velocity estimation in coherent radar system based on scaled radon fourier transform," *IEEE Transactions on Vehicular Technology*, vol. 69, no. 6, pp. 6525–6540, 2020.

[7] Othmar Frey and Erich Meier, "3-D time-domain sar imaging of a forest using airborne multibaseline data at L- and P-Bands," *IEEE Transactions on Geoscience and Remote Sensing*, vol. 49, no. 10, pp. 3660–3664, 2011.

[8] Simone Baffelli, Othmar Frey, and Irena Hajnsek, "Polarimetric analysis of natural terrain observed with a Ku-Band terrestrial radar," *IEEE Journal of Selected Topics in Applied Earth Observations and Remote Sensing*, vol. 12, no. 12, pp. 5268–5288, 2019.

[9] Gerhard Krieger, Alberto Moreira, Hauke Fiedler, Irena Hajnsek, Marian Werner, Marwan Younis, and Manfred Zink, "TanDEM-X: A satellite formation for high-resolution SAR interferometry," *IEEE Transactions on Geoscience and Remote Sensing*, vol. 45, no. 11, pp. 3317–3341, 2007.

[10] I. G. Cumming and F. H. Wong, "Digital signal processing of synthetic aperture radar data: Algorithms and implementation," 2004.

[11] Yongchao Zhang, Jiawei Luo, Jie Li, Deqing Mao, Yin Zhang, Yulin Huang, and Jianyu Yang, "Fast inverse-scattering reconstruction for airborne high-squint radar imagery based on doppler centroid compensation," *IEEE Transactions on Geoscience and Remote Sensing*, pp. 1–17, 2021.

[12] Jingyue Lu, Lei Zhang, Yan Huang, and Yunhe Cao, "High-resolution forward-looking multichannel SAR imagery with array deviation angle calibration," *IEEE Transactions on Geoscience and Remote Sensing*, vol. 58, no. 10, pp. 6914–6928, 2020.

[13] Yin Zhang, Deqing Mao, Yongchao Zhang, Yulin Huang, and Jianyu Yang, "Multi-beam Doppler beam sharpening approach for airborne forward-looking radar imaging," in *2017 IEEE International Geoscience and Remote Sensing Symposium (IGARSS)*, 2017, pp. 6142–6145.

[14] G. Krieger and A. Moreira, "Multistatic SAR satellite formations: potentials and challenges," in *Proceedings. 2005 IEEE International Geoscience and Remote Sensing Symposium, 2005. IGARSS '05.*, 2005, vol. 4, pp. 2680–2684.

This article has been accepted for publication in a future issue of this journal, but has not been fully edited. Content may change prior to final publication. Citation information: DOI 10.1109/JSTARS.2021.3106449, IEEE Journal of Selected Topics in Applied Earth Observations and Remote Sensing

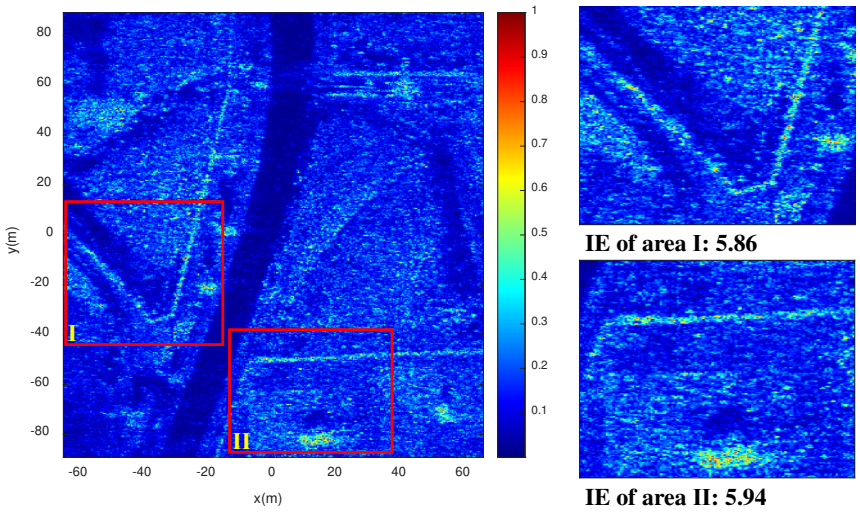

(a)

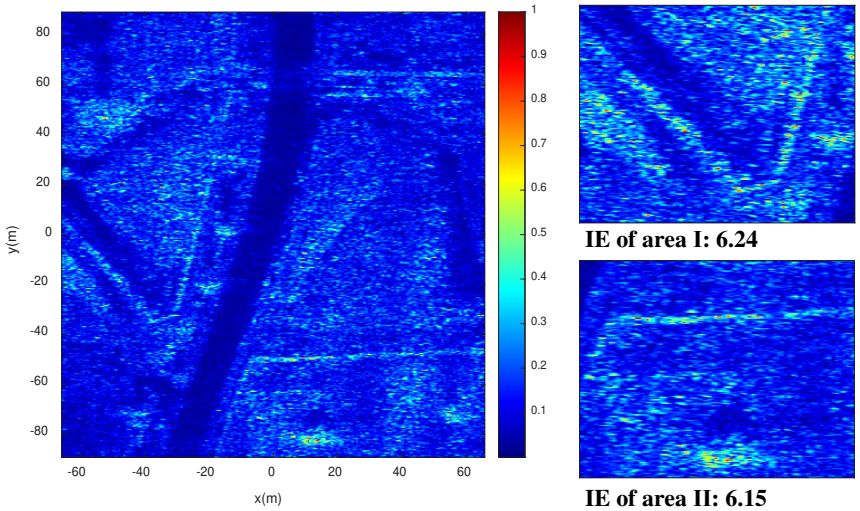

(b)

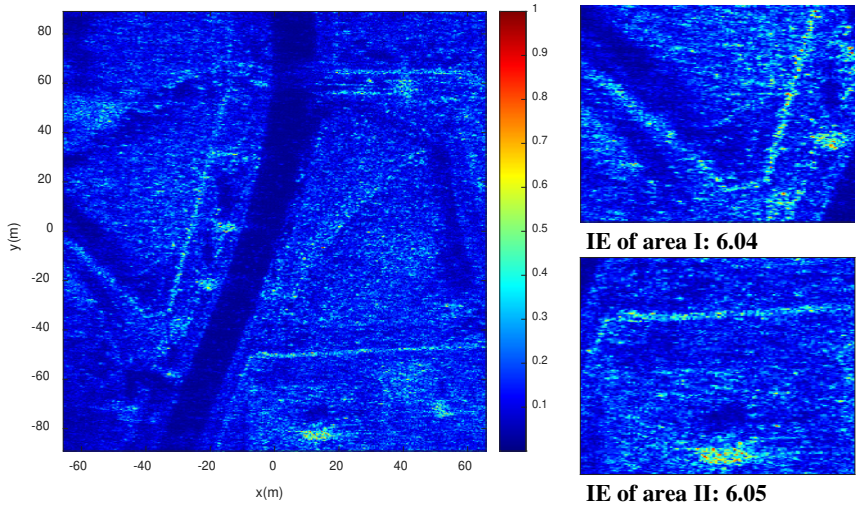

(c)

Fig. 11. Simulated results for 2-D scenario. (a) 2-D scenario imaging result of Path A. (b) 2-D scenario target imaging result of Path B. (c) 2-D scenario target imaging result of Path C.

[15] Jonathan D. Coker and Ahmed H. Tewfik, "Multistatic SAR image reconstruction based on an elliptical-geometry radon transform," in *2007 International Waveform Diversity and Design Conference*, 2007, pp. 204–208.

[16] B.D. Rigling and R.L. Moses, "Three-dimensional surface reconstruction from multistatic SAR images," *IEEE Transactions on Image Processing*, vol. 14, no. 8, pp. 1159–1171, 2005.

[17] Yanping Li, Zhenhua Zhang, Mengdao Xing, and Zheng Bao, "Bistatic spotlight SAR processing using the frequency-scaling algorithm," *IEEE Geoscience and Remote Sensing Letters*, vol. 5, no. 1, pp. 48–52, 2008.

[18] Michail Antoniou and Mikhail Cherniakov, "Gnss-based bistatic sar: A signal processing view," *EURASIP Journal on Advances in Signal Processing*, vol. 2013, no. 1, pp. 1–16, 2013.

[19] Fabrizio Santi, Michail Antoniou, and Debora Pastina, "Point spread function analysis for gnss-based multistatic SAR," *IEEE Geoscience and Remote Sensing Letters*, vol. 12, no. 2, pp. 304–308, 2015.

[20] Fabrizio Santi, Marta Bucciarelli, Debora Pastina, Michail Antoniou, and Mikhail Cherniakov, "Spatial resolution improvement in GNSS-Based SAR using multistatic acquisitions and feature extraction," *IEEE Transactions on Geoscience and Remote Sensing*, vol. 54, no. 10, pp. 6217–6231, 2016.

[21] Fanyun Xu, Rufei Wang, Junyu Zhu, Yongchao Zhang, Yin Zhang, Yulin Huang, and Jianyu Yang, "Topology design for distributed radar imaging based on wavenumber domain splicing analysis," in *2020 IEEE Radar Conference (RadarConf20)*, 2020, pp. 1–6.

[22] Jianping Wang, Pascal Aubry, and Alexander Yarovoy, "Wavenumber-domain multiband signal fusion with matrix-pencil approach for high-resolution imaging," *IEEE Transactions on Geoscience and Remote Sensing*, vol. 56, no. 7, pp. 4037–4049, 2018.

[23] Yao Cheng, Shunsheng Zhang, Bingji Zhao, and Cheng Hu, "SA-based orbital design method for GEO-BiSAR resolution improvement," in *2017 XXXIInd General Assembly and Scientific Symposium of the International Union of Radio Science (URSI GASS)*, 2017, pp. 1–4.

[24] Yong Zou, Xun Gao, Xiang Li, and Yong Liu, "A matrix pencil algorithm based multiband iterative fusion imaging method," *Scientific Reports*, vol. 6, pp. 19440, 01 2016.

[25] Ursula Gessner, Miriam Machwitz, Thomas Esch, Adina Bertram, Vahid Naeimi, Claudia Kuenzer, and Stefan Dech, "Multi-sensor mapping of west african land cover using MODIS, ASAR and TanDEM-X/TerraSAR-X data," *Remote Sensing of Environment*, vol. 164, 04 2015.

[26] T. Derham, S. Doughty, C. Baker, and K. Woodbridge, "Ambiguity functions for spatially coherent and incoherent multistatic radar," *IEEE Transactions on Aerospace and Electronic Systems*, vol. 46, no. 1, pp. 230–245, 2010.

[27] William Dower and Mark Yeary, "Bistatic SAR: Forecasting spatial resolution," *IEEE Transactions on Aerospace and Electronic Systems*, vol. 55, no. 4, pp. 1584–1595, 2019.

[28] Tao Zeng, M. Cherniakov, and Teng Long, "Generalized approach to resolution analysis in BSAR," *IEEE Transactions on Aerospace and Electronic Systems*, vol. 41, no. 2, pp. 461–474, 2005.

[29] Hee-Sub Shin and Jong-Tae Lim, "Omega-k algorithm for airborne forward-looking bistatic spotlight SAR imaging," *IEEE Geoscience and Remote Sensing Letters*, vol. 6, no. 2, pp. 312–316, 2009.

[30] A. Reigber, A. Moreira, and K.P. Papathanassiou, "First demonstration of airborne SAR tomography using multibaseline l-band data," in *IEEE 1999 International Geoscience and Remote Sensing Symposium. IGARSS'99 (Cat. No.99CH36293)*, 1999, vol. 1, pp. 44–46 vol.1.

[31] Xiaolong Li, Zhi Sun, Tianxian Zhang, Wei Yi, Guolong Cui, and Lingjiang Kong, "Wrfrft-based coherent detection and parameter estimation of radar moving target with unknown entry/departure time," *Signal Processing*, vol. 166, pp. 107228, 2020.

[32] Zhiwei Xu and Daiyin Zhu, "High-resolution miniature UAV SAR imaging based on GPU architecture," *Journal of Physics: Conference Series*, vol. 1074, pp. 012122, 09 2018.

[33] Lei Yang, Song Zhou, Lifan Zhao, and Guoan Bi, "Forward velocity extraction from UAV spotlight SAR data," in *2017 IEEE Radio and Antenna Days of the Indian Ocean (RADIO)*, 2017, pp. 1–3.

[34] Yan Cao, Wanyu Wei, Yu Bai, and Hu Qiao, "Multi-base multi-UAV cooperative reconnaissance path planning with genetic algorithm," *Cluster Computing*, vol. 22, 05 2019.

[35] Ilaria Catapano, Gianluca Gennarelli, Giovanni Ludeno, Carlo Noviello, Giuseppe Esposito, Alfredo Renga, Giancarmine Fasano, and F. Soldovieri, "Small Multicopter-UAV-Based radar imaging: Performance assessment for a single flight track," *Remote Sensing*, vol. 12, pp. 774, 02 2020.

[36] Lei Zhang, Zhijun Qiao, Meng-dao Xing, Lei Yang, and Zheng Bao, "A robust motion compensation approach for UAV SAR imagery," *IEEE Transactions on Geoscience and Remote Sensing*, vol. 50, no. 8, pp. 3202–3218, 2012.

[37] R. Abraham Martin, Landen Blackburn, Joshua Pulsipher, Kevin Franke, and John D. Hedengren, "Potential benefits of combining anomaly detection with view planning for UAV infrastructure modeling," *Remote Sensing*, vol. 9, no. 5, 2017.

[38] A. Cilek, S. Berberoglu, C. Donmez, and M. Nal, "Generation of high-resolution 3-D maps for landscape planning and design using UAV technologies," 2020.

[39] Johan Karlsson, William Rowe, Luzhou Xu, George-Othon Glentis, and Jian Li, "Fast missing-data IAA with application to notched spectrum SAR," *IEEE Transactions on Aerospace and Electronic Systems*, vol. 50, no. 2, pp. 959–971, 2014.

[40] Sonia Tomei, Alessio Bacci, Elisa Giusti, Marco Martorella, and Fabrizio Berizzi, "Compressive sensing-based inverse synthetic radar imaging imaging from incomplete data," *IET Radar, Sonar & Navigation*, vol. 10, no. 2, pp. 386–397, 2016.

[41] Deqing Mao, Yongchao Zhang, Yin Zhang, Weibo Huo, Jifang Pei, and Yulin Huang, "Target fast reconstruction of real aperture radar using data extrapolation-based parallel iterative adaptive approach," *IEEE Journal of Selected Topics in Applied Earth Observations and Remote Sensing*, vol. 14, pp. 2258–2269, 2021.

[42] Othmar Frey, Christophe Magnard, Maurice Ruegg, and Erich Meier, "Focusing of airborne synthetic aperture radar data from highly non-linear flight tracks," *IEEE Transactions on Geoscience and Remote Sensing*, vol. 47, no. 6, pp. 1844–1858, 2009.

[43] Jianlai Chen, Mengdao Xing, Xiang-Gen Xia, Junchao Zhang, Buge Liang, and De-Gui Yang, "SVD-Based ambiguity function analysis for nonlinear trajectory SAR," *IEEE Transactions on Geoscience and Remote Sensing*, vol. 59, no. 4, pp. 3072–3087, 2021.

[44] Flavia Causa, Giancarmine Fasano, and Michele Grassi, "Multi-UAV path planning for autonomous missions in mixed GNSS coverage scenarios," *Sensors*, vol. 18, pp. 4188, 11 2018.

[45] Anargyros Kostaras, Ioannis Nikolos, Nikos Tsourveloudis, and Kimon Valavanis, "Evolutionary algorithm based on-line path planner for UAV navigation.," 04 2021.

[46] Changwen Zheng, Lei Li, Fanjiang Xu, Fuchun Sun, and Mingyue Ding, "Evolutionary route planner for unmanned air vehicles," *IEEE Transactions on Robotics*, vol. 21, no. 4, pp. 609–620, 2005.

[47] Alberto Pretto, Stephanie Aravecchia, Wolfram Burgard, Nived Chebrolu, Christian Dornhege, Tillmann Falck, Freya Veronika Fleckenstein, Alessandra Fontenla, Marco Imperoli, Raghav Khanna, Frank Liebisch, Philipp Lottes, Andres Milioto, Daniele Nardi, Sandro Nardi, Johannes Pfeifer, Marija Popovic, Ciro Potena, Cedric Pradalier, Elisa Rothacker-Feder, Inkyu Sa, Alexander Schaefer, Roland Siegwart, Cyrill Stachniss, Achim Walter, Wera Winterhalter, Xiaolong Wu, and Juan Nieto, "Building an aerial-ground robotics system for precision farming: An adaptable solution," *IEEE Robotics Automation Magazine*, pp. 0–0, 2020.

[48] Yangguang Fu, Mingyue Ding, Chengping Zhou, and Hanping Hu, "Route planning for unmanned aerial vehicle (UAV) on the sea using hybrid differential evolution and quantum-behaved particle swarm optimization," *IEEE Transactions on Systems, Man, and Cybernetics: Systems*, vol. 43, no. 6, pp. 1451–1465, 2013.

[49] Stanisław Konatowski and Piotr Pawłowski, "Ant colony optimization algorithm for UAV path planning," in *2018 14th International Conference on Advanced Trends in Radioelecrtronics, Telecommunications and Computer Engineering (TCSET)*, 2018, pp. 177–182.

[50] Zhichao Sun, Junjie Wu, Jianyu Yang, Yulin Huang, Caipin Li, and Dongtao Li, "Path planning for GEO-UAV bistatic SAR using constrained adaptive multiobjective differential evolution," *IEEE Transactions on Geoscience and Remote Sensing*, vol. 54, no. 11, pp. 6444–6457, 2016.

[51] Vincent Roberge, Mohammed Tarbouchi, and Gilles Labonte, "Comparison of parallel genetic algorithm and particle swarm optimization for real-time UAV path planning," *IEEE Transactions on Industrial Informatics*, vol. 9, no. 1, pp. 132–141, 2013.

[52] Fanyun Xu, Rufei Wang, Lu Zhao, Yongchao Zhang, Yin Zhang, Yulin Huang, and Jianyu Yang, "Uav intelligent optimal path planning method for distributed radar short-time aperture synthesis," in *IGARSS 2020 - 2020 IEEE International Geoscience and Remote Sensing Symposium*, 2020, pp. 469–472.

[53] Deqing Mao, Yongchao Zhang, Jifang Pei, Weibo Huo, Yin Zhang, Yulin Huang, and Jianyu Yang, "Forward-looking geometric configuration optimization design for spaceborne-airborne multistatic synthetic aperture

radar," *IEEE Journal of Selected Topics in Applied Earth Observations and Remote Sensing*, 2021, 10.1109/JSTARS.2021.3103802.

[54] Zhixi Li and Ram M. Narayanan, "Data level fusion of multilook inverse synthetic aperture radar (isar) images," in *35th IEEE Applied Imagery and Pattern Recognition Workshop (AIPR'06)*, 2006, pp. 2–2.

[55] Yongchao Zhang, Jiawei Luo, Jie Li, Deqing Mao, Yin Zhang, Yulin Huang, and Jianyu Yang, "Fast inverse-scattering reconstruction for airborne high-squint radar imagery based on doppler centroid compensation," *IEEE Transactions on Geoscience and Remote Sensing*, pp. 1–17, 2021.

[56] Sky McKinley and Megan Levine, "Cubic spline interpolation," *College of the Redwoods*, vol. 45, no. 1, pp. 1049–1060, 1998.

[57] B.D. Rigling and R.L. Moses, "Polar format algorithm for bistatic SAR," *IEEE Transactions on Aerospace and Electronic Systems*, vol. 40, no. 4, pp. 1147–1159, 2004.

[58] Yuxuan Miao, Junjie Wu, Zhongyu Li, and Jianyu Yang, "A generalized wavefront-curvature-corrected polar format algorithm to focus bistatic SAR under complicated flight paths," *IEEE Journal of Selected Topics in Applied Earth Observations and Remote Sensing*, vol. 13, pp. 3757–3771, 2020.

[59] Hongyang An, Junjie Wu, Zhichao Sun, Jianyu Yang, Yulin Huang, and Haiguang Yang, "Topology design for geosynchronous spaceborne–airborne multistatic SAR," *IEEE Geoscience and Remote Sensing Letters*, vol. 15, no. 11, pp. 1715–1719, 2018.

Fanyun Xu (S'18) received the B.S. degree in Electronic Information Engineering from University of Electronic Science and Technology of China (UESTC), Chengdu, China, in 2017. Currently, he is pursuing the Ph.D. degree with the School of Information and Communication Engineering, UESTC, Chengdu, China.

His research interests include distributed radar and radar signal processing.

Yongchao Zhang (S'15-M'18) received the B.S. degree in electronic information engineering from Hainan University, Haikou, China, in 2011. He received the Ph.D. degree from the School of Information and Communication Engineering, University of Electronic Science and Technology of China (UESTC), Chengdu, China, in 2018. From 2016 to 2017, he was a Visiting Student with the Lund University, Lund, Sweden. He is currently an Associate Research Fellow with the School of Information and Communication Engineering, UESTC.

His research interests include array signal processing and inverse problem in radar applications.

Rufei Wang (S'18) received the B.S. degree in Electronic Information Engineering from Ocean University of China (OUC), Qingdao, China, in 2017.

She is currently working toward the Ph.D. degree with the School of Information and Communication Engineering, University of Electronic Science and Technology of China (UESTC), Chengdu, China.

Her research interests include radar signal processing and radar target detection.

Chenyang Mi Received the B.S. degree in Electronic Information Engineering from University of Electronic Science and Technology of China (UESTC), Chengdu, China, in 2020. Currently, he is pursuing the M.S. degree with the School of Information and Communication Engineering, UESTC, Chengdu, China.

His research interests include distributed radar and radar signal processing.

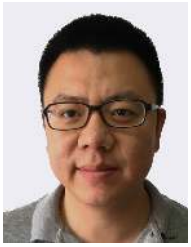

Yin Zhang (S'13-M'17) received the B.S. and Ph.D. degrees in electronic information engineering from University of Electronic Science and Technology of China (UESTC), Chengdu, China, in 2008 and 2016, respectively. From 2015 to 2016, he was a visiting student at University of Delaware, USA. Currently, he is an associate research fellow with the School of Information and Communication Engineering, UESTC.

His research interests include radar imaging and signal processing in related radar applications.

Yulin Huang (M'08-SM'17) received the B.S. and Ph.D. degrees in electronic engineering from the University of Electronic Science and Technology of China (UESTC), Chengdu, China, in 2002, and 2008, respectively. From 2013 to 2014, he was a visiting researcher at University of Houston, USA. Since 2016, he has been a Professor with the School of Information and Communication Engineering, UESTC.

Dr. Huang has authored more than 80 journal and conference papers. He is also a member of the IEEE Aerospace and Electronic Systems Society. His research interests include synthetic aperture radar, target detection and recognition, artificial intelligence and machine Learning.

Jianyu Yang (M'91) received the B.S. degree from the National University of Defense Technology, Changsha, China, in 1984, and the M.S. and Ph.D. degrees from the University of Electronic Science and Technology of China (UESTC), Chengdu, in 1987 and 1991, respectively. In 2005, he visited Massachusetts Institute of Technology, USA. Since 1999, he has been a Professor with the School of Information and Communication Engineering, UESTC.

Dr. Yang has authored more than 120 journal and conference papers. He is a Fellow of the Chinese Institute of Electronics. His research interests are mainly in synthetic aperture radar and statistical signal processing.